Size effects on the plastic shock formation in steady-state cavity expansion in porous ductile materials

T. dos Santos[a,*], J. A. Rodríguez-Martínez[b]

[a] *Departamento de Engenharia Mecânica, Universidade Federal de Santa Maria, Av. Roraima, 1000, Prédio 7, Santa Maria, RS, 97105-900, Brazil.*
[b] *Department of Continuum Mechanics and Structural Analysis, University Carlos III of Madrid, Avda. de la Universidad, 30, 28911 Leganés, Madrid, Spain*

Abstract

In this paper, we have studied the hypervelocity expansion of a spherical cavity in an infinite medium modeled with the extension of the porous plasticity criterion of Gurson [23] developed by Chen and Yuan [7] to account for plastic strain gradient induced size effects. Following the self-similar, steady-state solution derived by Cohen and Durban [9] for size-independent porous materials, we have computed the critical cavity expansion velocity which leads to the emergence of plastic shock waves for a wide range of initial void volume fractions and different values of the length scale parameter that controls the effect of size. We have shown that size effects hinder the emergence of plastic shock waves, so that as the length scale parameter increases, the expansion velocity required for the plastic shock to be formed increases. In addition, while porosity favors the formation of plastic shocks, as shown by Cohen and Durban [9], our results indicate that the effect of initial void volume fraction on plastic shock wave formation decreases for size-dependent materials.

Keywords:
Dynamic cavity expansion, Porous plasticity, Size effects, Plastic shock waves

1. Introduction

High-velocity impact of small particles onto mechanical structures has been an important concern in many engineering applications in the past decades [15, 51]. Specifically in aerospace industry, the degradation of engine components and protection shields due to high-velocity collision with small particles and debris has been intensively investigated in order to understand and avoid associated structural failure [11, 6]. In the specific scenario of the high-velocity impact of small hard particles onto metallic materials, two main features are expected to play major roles: (i) size effects due to small-sized indentations [37, 32, 36]; and (ii) shock wave propagation caused by high velocity impact [10, 9].

From a experimental point of view, Mok and Duffy [33] were the first authors to show that the results of dynamic indentation tests can be interpreted to provide a measure of the yield stress of metals over a range of strains taking into account the influence of strain-rate. Their work paved the way to subsequent studies using macro [45, 43, 28] and micro/nano [46, 5, 21, 38] tests to assess the mechanics of high strain-rate indentation and penetration of metallic materials. In this context, Hassani et al. [24] have recently developed an experimental setup to perform micro-particle impact indentation to determine material hardness at strain-rates beyond $10^6\,\mathrm{s}^{-1}$. These authors employed laser ablation to impact ceramic alumina micro-particles of $14\,\mu$m diameter onto copper and iron targets, and obtained time-resolved measurements of the impact and rebound velocities together with post-impact measurements of the size and volume of the indent.

On the modeling side, after the works of Hopkins [26] and Goodier [22], cavity expansion theories have been widely applied and considered as a simple and accurate tool to model the mechanics of indentation [27, 18, 20] and penetration [19, 16, 31] of metallic targets. In a context in which porous metallic materials are increasingly used in aerospace and aircraft industries (e.g. aircraft structures manufactured with 3D printed metallic materials [44, 50]), special attention shall be given to the hypervelocity cavity expansion model developed by Cohen and Durban [9] for elastoplastic porous ductile materials. They showed that material porosity favors the development of plastic shock waves and that the level of discontinuities induced by the plastic shock increases with the void volume fraction. These findings were also evidenced by dos Santos et al. [40] using finite element simulations. Moreover, Cleja-Tigoiu et al. [8] developed a rate-dependent cavity model to address hypervelocity penetration in porous concrete structures. Recently, the model of Cohen and Durban [9] has been extended by dos Santos et al. [41] in an effort to account for plastic strain gradient induced size effects on the dynamic micro-indentation of porous materials. As a subsequent study, this work uses the formulation of dos Santos et al. [41] to elucidate the effects of size and material porosity on the formation of plastic shocks emerging during hypervelocity cavitation of porous solids.

2. Constitutive framework

The constitutive framework is the same used in the recent paper of dos Santos et al. [41]. The rate of deformation tensor is considered to be the sum of an elastic part, $\boldsymbol{d}^e$, and a plastic part, $\boldsymbol{d}^p$:

$$\boldsymbol{d} = \boldsymbol{d}^e + \boldsymbol{d}^p \tag{1}$$

The elastic part is related to the rate of the Cauchy stress tensor $\boldsymbol{\sigma}$ by the following hypo-elastic law:

$$\overset{\triangledown}{\boldsymbol{\sigma}} = \boldsymbol{C} : \boldsymbol{d}^e \tag{2}$$

where $\overset{\triangledown}{()}$ denotes an objective derivative and $\boldsymbol{C}$ is the fourth-order isotropic elastic tensor:

*Corresponding author
Email address: tiago.santos@ufsm.br (T. dos Santos)

$$\boldsymbol{C} = \frac{E}{1+\nu}\boldsymbol{I}' + \frac{E}{3(1-2\nu)}\boldsymbol{1}\otimes\boldsymbol{1} \tag{3}$$

where E and ν are the Young's modulus and the Poisson's ratio, respectively, $\boldsymbol{1}$ is the unit second-order tensor and $\boldsymbol{I}'$ is the unit deviatoric fourth-order tensor.

The plastic part of the rate of deformation tensor is:

$$\boldsymbol{d}^p = \dot{\lambda}\frac{\partial\Phi}{\partial\boldsymbol{\sigma}} \tag{4}$$

where $\dot{\lambda}$ is a non-negative plastic multiplier and Φ is the plastic flow potential [23, 48, 49]:

$$\Phi = \left(\frac{\sigma_e}{\bar{\sigma}}\right)^2 + 2q_1 f\cosh\left(\frac{3q_2\sigma_h}{2\bar{\sigma}}\right) - 1 - (q_1 f)^2 \leq 0 \tag{5}$$

where q_1 and q_2 are material parameters and f is the void volume fraction (see equation (9)). The effective von Mises stress σ_e and the hydrostatic stress σ_h are:

$$\sigma_e = \sqrt{\frac{3}{2}\boldsymbol{s}:\boldsymbol{s}}, \quad \sigma_h = \frac{1}{3}\boldsymbol{\sigma}:\boldsymbol{1}, \quad \boldsymbol{s} = \boldsymbol{\sigma} - \sigma_h\boldsymbol{1}$$

with $\boldsymbol{s}$ being the deviatoric part of the Cauchy stress tensor. Similarly to Chen and Yuan [7], the flow strength of the matrix material $\bar{\sigma}$ is defined using a simple form of the generalized gradient plasticity model developed by Aifantis and co-workers [2, 3, 4, 47]:

$$\bar{\sigma} = \bar{\sigma}_{hom} + l\,E\,\|\nabla\bar{\varepsilon}^p\| \tag{6}$$

where l is the length scale parameter and $\|\nabla\bar{\varepsilon}^p\| = \left(\nabla\bar{\varepsilon}^p\cdot\nabla\bar{\varepsilon}^p\right)^{\frac{1}{2}}$, with $\bar{\varepsilon}^p = \int_0^t \dot{\bar{\varepsilon}}^p(\tau)\,d\tau$ being the effective plastic strain in the matrix material and $\dot{\bar{\varepsilon}}^p$ the effective plastic strain rate. To be emphasized that the constitutive relation adopted in Eq. (6) intends to mimic plastic strain gradient induced size effects, which arise in polycrystalline metals. Therefore, the length scale parameter l may be related to microstructure aspects, such as the material grain size and the accumulation of geometrically necessary dislocations [17, 36]. Moreover, $\bar{\sigma}_{hom}$ in Eq. (6) is the flow strength for homogeneous deformation:

$$\bar{\sigma}_{hom} = \sigma_0\left(1 + \frac{\bar{\varepsilon}^p}{\varepsilon_0}\right)^n \tag{7}$$

where σ_0 is the initial yield stress of the matrix material, n is the strain hardening exponent and ε_0 is the reference strain.

The equality between the rates of macroscopic plastic work and matrix plastic work [7]:

$$\boldsymbol{\sigma}:\boldsymbol{d}^p = (1-f)\,\bar{\sigma}\dot{\bar{\varepsilon}}^p \tag{8}$$

provides a relation between the plastic part of the rate of deformation tensor and the effective plastic strain rate in the matrix material.

Moreover, the evolution of the void volume fraction is:

$$\dot{f} = (1-f)\,\boldsymbol{d}^p:\boldsymbol{1} \tag{9}$$

The values of the parameters of the constitutive model, which are based on [42, 40], are given in Table 1.

Symbol	Property and units	Value
ρ_0	Initial density (kg/m^3)	7600
E	Young's modulus (GPa), Eq. (3)	70
ν	Poisson's ratio, Eq. (3)	0.3
q_1	Material parameter, Eq. (5)	1.25
q_2	Material parameter, Eq. (5)	1.0
σ_0	Initial yield stress (MPa), Eq. (7)	300
n	Strain hardening exponent, Eq. (7)	0.1
ε_0	Reference strain, Eq. (7)	0.00429

Table 1: Constitutive model parameters [42, 40].

3. Dynamic spherical cavity expansion model

Dynamic spherical cavity expansion theories have been widely accepted as a basic physical model underlying indentation and penetration mechanics in metallic materials [18, 29]. The problem studied is that of a pressurized spherical cavity of instantaneous radius a expanding under self-similar, steady-state conditions in an infinite medium described with the constitutive framework of Section 2. Following Masri and Durban [30] and Durban and Masri [16], the cavity expansion model is formulated using an Eulerian spherical system of coordinates (r, θ, ϕ) with origin located at the center of the cavity denoted by O in Fig. 1. The only independent variable is the non-dimensional radial coordinate $\xi = r/a$, so that the derivative with respect to r is:

$$\frac{\partial\,()}{\partial r} = \frac{\partial\,()}{\partial\xi}\frac{\partial\xi}{\partial r} = ()'\,\frac{1}{a} \tag{10}$$

where the prime superscript denotes differentiation with respect to ξ, and the time derivative is:

$$\dot{()} = \frac{\partial\,()}{\partial\xi}\dot{\xi} = ()'\,\frac{\dot{a}}{a}(v - \xi) \tag{11}$$

where $v = \dot{r}/\dot{a}$ is the dimensionless radial velocity.

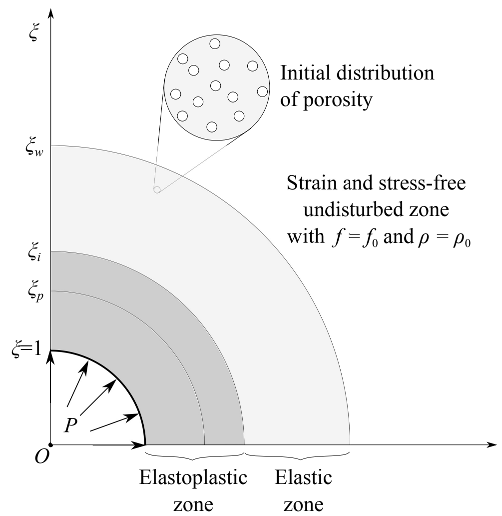

Figure 1: Illustration of the self-similar, steady-state cavity expansion field. The internal pressure p is applied at the cavity wall where $\xi = 1$. The remote region $\xi > \xi_w$ is a strain and stress-free undisturbed zone with $f = f_0$ and $\rho = \rho_0$. The elastic wave front is denoted by $\xi = \xi_w$, the transition between the elastic and elastoplastic regions by ξ_i, and the shock wave location by ξ_p. This figure is adapted from Durban and Masri [16].

Owing to the spherical symmetry of the problem, the only non-zero components of the Cauchy stress tensor are normal stresses along the radial, σ_{rr}, circumferential and azimuthal,

$\sigma_{\theta\theta} = \sigma_{\phi\phi}$, directions. Therefore, the Eulerian version of the balance of linear momentum reduces to:

$$\frac{\partial \sigma_{rr}}{\partial r} + \frac{2}{r}\left(\sigma_{rr} - \sigma_{\theta\theta}\right) = \rho \ddot{r} \tag{12}$$

where ρ is the current material density.

Employing Eqs. (10) and (11), previous expression becomes:

$$\left(\Sigma_{rr}\right)' + \frac{2}{\xi}\left(\Sigma_{rr} - \Sigma_{\theta\theta}\right) = m^2 \frac{\rho}{\rho_0}\left(v - \xi\right) v' \tag{13}$$

where $\Sigma_{rr} = \frac{\sigma_{rr}}{E}$ and $\Sigma_{\theta\theta} = \frac{\sigma_{\theta\theta}}{E}$ are dimensionless stresses, and $m = \frac{\dot{a}}{\sqrt{E/\rho_0}}$ is the dimensionless cavity expansion velocity, which is assumed to be constant in this steady-state problem.

Moreover, the non-zero components of the strain rate tensor are:

$$d_{rr} = \frac{\partial \dot{r}}{\partial r} = \frac{\dot{a}}{a} v' \tag{14}$$

$$d_{\theta\theta} = d_{\phi\phi} = \frac{\dot{r}}{r} = \frac{\dot{a}}{a}\frac{v}{\xi} \tag{15}$$

where Eqs. (10) and (11) have been employed. The hypo-elastic law introduced in equation (2) can be rewritten as:

$$d^e_{rr} = \frac{\dot{\sigma}_{rr}}{E} - \frac{2\nu\dot{\sigma}_{\theta\theta}}{E} \tag{16}$$

$$d^e_{\theta\theta} = d^e_{\phi\phi} = \frac{\left(1-\nu\right)\dot{\sigma}_{\theta\theta}}{E} - \frac{\nu\dot{\sigma}_{rr}}{E} \tag{17}$$

Notice that, in absence of material spin, the objective derivative $\overset{\triangledown}{()}$, see equation (2), has been replaced by a simple time derivative $\dot{()}$.

Furthermore, considering the flow rule (4), the flow potential (5) and relation (8), the active plastic deformation rates are:

$$d^p_{rr} = \left(1-f\right)\dot{\bar{\varepsilon}}^P \tilde{N}_{rr} \tag{18}$$

$$d^p_{\theta\theta} = d^p_{\phi\phi} = \left(1-f\right)\dot{\bar{\varepsilon}}^P \tilde{N}_{\theta\theta} \tag{19}$$

with

$$\tilde{N}_{rr} = \frac{1}{2}\frac{-2\frac{\Sigma_e}{\bar{\Sigma}} + q_1 q_2 f \sinh\left(\frac{3q_2\Sigma_h}{2\bar{\Sigma}}\right)}{\left(\frac{\Sigma_e}{\bar{\Sigma}}\right)^2 + q_1 q_2 f \sinh\left(\frac{3q_2\Sigma_h}{2\bar{\Sigma}}\right)\frac{3\Sigma_h}{2\bar{\Sigma}}} \tag{20}$$

$$\tilde{N}_{\theta\theta} = \frac{1}{2}\frac{\frac{\Sigma_e}{\bar{\Sigma}} + q_1 q_2 f \sinh\left(\frac{3q_2\Sigma_h}{2\bar{\Sigma}}\right)}{\left(\frac{\Sigma_e}{\bar{\Sigma}}\right)^2 + q_1 q_2 f \sinh\left(\frac{3q_2\Sigma_h}{2\bar{\Sigma}}\right)\frac{3\Sigma_h}{2\bar{\Sigma}}} \tag{21}$$

where $\Sigma_e = \frac{\sigma_e}{E} = \frac{\sigma_{\theta\theta}-\sigma_{rr}}{E}$ is the dimensionless von Mises stress, $\bar{\Sigma} = \frac{\bar{\sigma}}{E}$ is the dimensionless matrix flow strength and $\Sigma_h = \frac{\sigma_h}{E}$ is the dimensionless hydrostatic stress.

Moreover, using equations (1), (14), (15), (18) and (19), the following expressions are obtained:

$$v' = \left(v - \xi\right)\left[\Sigma'_{rr} - 2\nu\Sigma'_{\theta\theta} + \left(1-f\right)\left(\bar{\varepsilon}^p\right)'\tilde{N}_{rr}\right] \tag{22}$$

$$\frac{v}{\xi} = \left(v - \xi\right)\left[-\nu\Sigma'_{rr} + \left(1-\nu\right)\Sigma'_{\theta\theta} + \left(1-f\right)\left(\bar{\varepsilon}^p\right)'\tilde{N}_{\theta\theta}\right] \tag{23}$$

For a spherically symmetric problem, using Eq. (10), the flow strength of the matrix material given in Eq. (6) becomes:

$$\bar{\Sigma} = \bar{\Sigma}_{hom} + \frac{l}{a}\left(\bar{\varepsilon}^p\right)' \tag{24}$$

where $\bar{\Sigma}_{hom} = \frac{\bar{\sigma}_{hom}}{E}$ is the dimensionless flow strength for homogeneous deformation given by (see Eq. (7)):

$$\bar{\Sigma}_{hom} = \Sigma_0\left(1 + \frac{\bar{\varepsilon}^p}{\varepsilon_0}\right)^n \tag{25}$$

with $\Sigma_0 = \frac{\sigma_0}{E}$ being the dimensionless initial yield stress of the matrix material. Equation (24) brings out that the effect of plastic strain gradients in the cavitation fields depends on the ratio between the length scale parameter l and the current cavity radius a, so that for $a \gg l$ the cavitation fields become size-independent (see Danas et al. [14]).

Moreover, using Eqs. (11), (18) and (19), the material porosity evolution, Eq. (9), becomes:

$$f' = \left(1-f\right)^2\left(\tilde{N}_{rr} + 2\tilde{N}_{\theta\theta}\right)\left(\bar{\varepsilon}^p\right)' \tag{26}$$

For a plastic loading, the relation between Σ_e and $\bar{\Sigma}$ is given when the flow potential, Eq. (5), is $\Phi = 0$:

$$\left(\frac{\Sigma_e}{\bar{\Sigma}}\right)^2 + 2q_1 f \cosh\left(\frac{3q_2\Sigma_h}{2\bar{\Sigma}}\right) - 1 - \left(q_1 f\right)^2 = 0 \tag{27}$$

Differentiating Eq. (27) with respect to ξ, using Eq. (26) and the relations $3\Sigma_h = \Sigma_{rr} + 2\Sigma_{\theta\theta}$ and $\Sigma_e = \Sigma_{\theta\theta} - \Sigma_{rr}$, the following expression is obtained:

$$\chi_1\Sigma'_{rr} + \chi_2\Sigma'_{\theta\theta} + \chi_3\bar{\Sigma}' + \chi_4\left(1-f\right)^2\left(\tilde{N}_{rr} + 2\tilde{N}_{\theta\theta}\right)\left(\bar{\varepsilon}^p\right)' = 0 \tag{28}$$

with

$$\chi_1 = \frac{1}{2}q_1 q_2 f \sinh\left(\frac{3q_2\Sigma_h}{2\bar{\Sigma}}\right) - \frac{\Sigma_e}{\bar{\Sigma}} \tag{29}$$

$$\chi_2 = q_1 q_2 f \sinh\left(\frac{3q_2\Sigma_h}{2\bar{\Sigma}}\right) + \frac{\Sigma_e}{\bar{\Sigma}} \tag{30}$$

$$\chi_3 = -q_1 f \sinh\left(\frac{3q_2\Sigma_h}{2\bar{\Sigma}}\right)\frac{3q_2\Sigma_h}{2\bar{\Sigma}} - \frac{\Sigma_e^2}{\bar{\Sigma}^2} \tag{31}$$

$$\chi_4 = q_1\left[\cosh\left(\frac{3q_2\Sigma_h}{2\bar{\Sigma}}\right) - q_1 f\right]\bar{\Sigma} \tag{32}$$

The material porosity is obtained solving Eq. (27) for the physical branch of f (see Cohen and Durban [9]):

$$f = \frac{1}{q_1}\left[\cosh\left(\frac{3q_2}{2}\frac{\Sigma_h}{\Sigma_y}\right) - \sqrt{\sinh^2\left(\frac{3q_2}{2}\frac{\Sigma_h}{\Sigma_y}\right) + \left(\frac{\Sigma_e}{\Sigma_y}\right)^2}\right] \tag{33}$$

Furthermore, the principle of mass conservation, in Eulerian description, yields:

$$\dot{\rho} + \rho\left(d_{rr} + 2d_{\theta\theta}\right) = 0 \tag{34}$$

Integration of previous expression, from a given coordinate ξ, to the elastic wave front ξ_w, using relations (1), (9), (11), (16) and (17), leads to:

$$\frac{\rho}{\rho_0} = \left(\frac{1-f}{1-f_0}\right)\exp\left[-3(1-2\nu)\Sigma_h\right] \tag{35}$$

where ρ_0 is the initial material density (see Table 1). Note that, in order to obtain previous expression, the conditions $f = f_0$, $\rho = \rho_0$ and $\Sigma_h = 0$ have been considered at $\xi = \xi_w$ (see Fig. 1).

In this model, Eqs. (13), (22), (23), (24), and (28), provide a system of differential equations with derivatives of five unknowns $\left(v, \Sigma_{rr}, \Sigma_{\theta\theta}, \bar{\Sigma}, \bar{\varepsilon}^p\right)$, with $\bar{\Sigma}_{hom}$, f and ρ being calculated from the algebraic relations (25), (33) and (35), respectively. The problem is completed with the following boundary conditions:

$$v = 1 \quad \text{and} \quad \Sigma_{rr} = -P, \quad \text{at} \quad \xi = 1 \tag{36}$$

and

$$v = 0, \quad \Sigma_{rr} = \Sigma_{\theta\theta} = 0, \quad \text{at} \quad \xi = \xi_w \tag{37}$$

where $P = \frac{p}{E}$ is the dimensionless applied pressure. The integration is performed over the independent variable ξ, from ξ_w up to $\xi = 1$ (see Fig. 1). An iterative shooting method is used to enforce the velocity boundary condition, while the stress boundary condition is used to calculate the corresponding applied pressure.

Moreover, we consider a shock to be formed when the following function:

$$\Delta = m^2 \frac{\rho}{\rho_0} (v - \xi)^2 - \frac{(1-f) \frac{\partial \bar{\varepsilon}^p}{\partial \bar{\Sigma}} \tilde{N}_{\theta\theta} \chi_2 - (1-\nu) \chi_5}{-(1-2\nu)(1+\nu) \chi_5 + \chi_6} \tag{38}$$

with

$$\chi_5 = \chi_3 + \chi_4 (1-f)^2 \left(\tilde{N}_{rr} + 2\tilde{N}_{\theta\theta}\right) \frac{\partial \bar{\varepsilon}^p}{\partial \bar{\Sigma}} \tag{39}$$

$$\chi_6 = (1-f) \frac{\partial \bar{\varepsilon}^p}{\partial \bar{\Sigma}} \left\{ \left[(1-\nu) \tilde{N}_{rr} + 4\nu \tilde{N}_{\theta\theta}\right] \chi_1 + \tilde{N}_{\theta\theta} \chi_2 \right\} \tag{40}$$

becomes zero, i.e. $\Delta = 0$ is the shock wave condition which serves to identify both the plastic shock and the elastic wave front (see Fig. 1). Hereinafter, Δ will be called shock wave function, and the dimensionless velocity for which the plastic shock wave emerges will be referred to as critical dimensionless velocity m_c. Note that expression (38) was derived by Cohen and Durban [9] for size and rate independent porous materials. Thus, for $l = 0$ (i.e. $\bar{\Sigma} = \bar{\Sigma}_{hom}$, see Eq. (24)) the derivative $\partial \bar{\varepsilon}^p / \partial \bar{\Sigma}$ can be calculated analytically using Eq. (25). In contrast, for $l > 0$, it has to be approximated numerically.

4. Results

Figure 2 shows the critical dimensionless velocity m_c versus the dimensionless length scale parameter l/a, for different initial porosities $f_0 = 0, 0.01, 0.05$ and 0.1. Exploring such a wide spectrum of initial void volume fractions helps to elucidate the role of porosity in the emergence of plastic shock waves, providing definite trends for the interplay between size effects and initial void volume fraction. In addition, note that it is relatively common that sintered and additively manufactured metals display levels of initial porosity between 1% and 10% (e.g. see Aboulkhair et al. [1] and Heidari et al. [25]), so that the range of void volume fractions investigated in this work can be representative of actual metallic materials. Moreover, the range of values investigated for the dimensionless length scale parameter $0 \leq l/a \leq 0.002$ is similar to that considered by dos Santos et al. [41]. The critical dimensionless velocity increases with the normalized length scale, bringing out that size effects hinder the emergence of plastic shocks. To the authors' knowledge, this is an original outcome of this paper. The explanation is that the plastic strain gradients introduced by equation (24) have a regularizing effect that prevents the development of singularities (we will further elaborate on this issue with the results presented in Fig. 5). On the other hand, the increase of initial porosity shifts the $m_c - l/a$ curves down, showing that porosity favors the formation of plastic shock waves (as demonstrated by Cohen and Durban [9]). Nevertheless, notice that the difference between the results obtained for different values of f_0 decreases with l/a, revealing that the influence of porosity on plastic shock wave formation is reduced as the effect of size increases. In fact, we have checked that for $l/a \geq 0.004$ the difference in the critical dimensionless velocity obtained for the fully dense material and the three initial void volume fractions considered is below 0.01. To the best of our knowledge, this is also an original contribution of this paper.

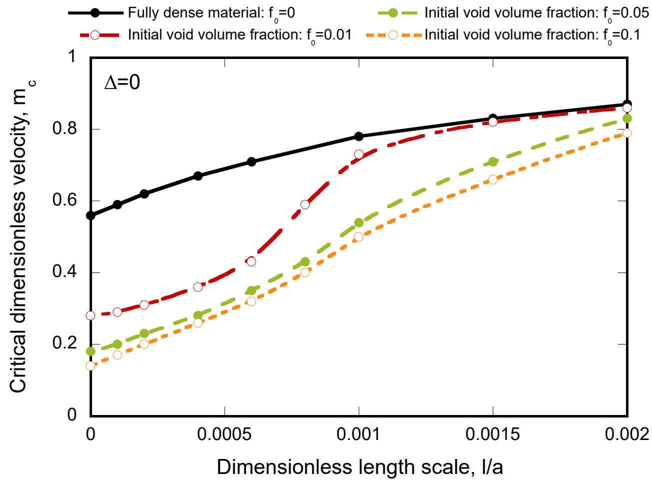

Figure 2: Evolution of the critical dimensionless velocity m_c for which the shock wave emerges ($\Delta = 0$) versus the dimensionless length scale l/a for $f_0 = 0$, 0.01, 0.05 and 0.1.

Figure 3 shows the evolution of the critical dimensionless velocity m_c with the initial porosity f_0, for different values of the dimensionless length scale parameter $l/a = 0$, 0.0004, 0.001 and 0.002. Consistent with the results pictured in Fig. 2, the porosity favors the emergence of plastic shocks, and increasing f_0 boosts the influence of the dimensionless length scale parameter on the critical velocity leading to shocks formation. For $l/a = 0$ and 0.0004 the $m_c - f_0$ curves display a concave-upwards shape, so that the critical dimensionless velocity decreases nonlinearly with the initial porosity, being the slope of the $m_c - f_0$ curves smaller as the initial porosity increases. In contrast, for $l/a = 0.002$ the decrease of the critical dimensionless velocity with the porosity is mild and roughly linear. To be highlighted that, for the rate independent material employed in this work, the only feature regularizing and delaying the shock wave formation is the plastic strain induced size effects. However, for rate dependent porous metals, viscous [34, 39] and micro-inertia induced pore size effects [12, 13] are also expected to attenuate plastic shock waves.

Figure 4 shows the evolution of the shock wave function Δ with the dimensionless radial coordinate ξ for different values of the dimensionless length scale $l/a = 0$, 0.0004, 0.001 and 0.002. Figure 4a displays results for the fully dense material $f_0 = 0$ and $m = 0.55$. This value of m is slightly lower than m_c for $f_0 = 0$ and $l/a = 0$ (size-independent material). The shape of the $\Delta - \xi$ curves is similar for all the dimensionless length scale parameters. The function Δ first increases, reaches a maximum, drops rapidly and then increases again. The first maximum corresponds to the elastic/elastoplastic interface ξ_i. The zoomed area in the right upper part of the plot shows that it is only for the size-independent material for which the shock wave emergence condition $\Delta \to 0$ is met (the plastic shock is located at the elastic/elastoplastic interface for the material with $l/a = 0$). For the size-dependent materials, $l/a > 0$, the

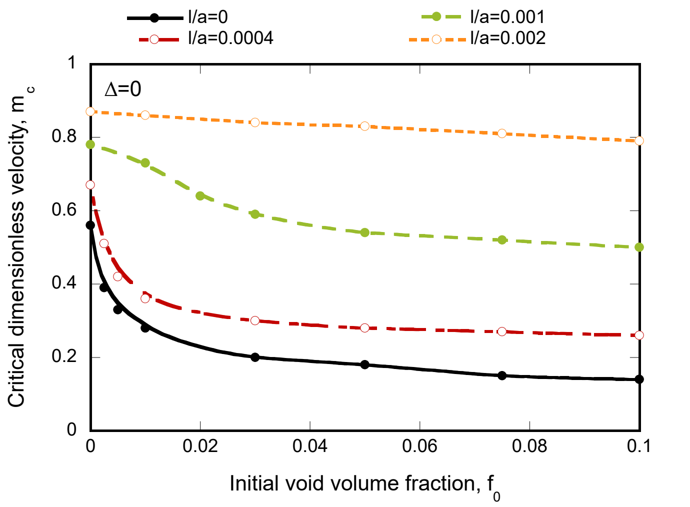

Figure 3: Evolution of the critical dimensionless velocity m_c for which the shock wave emerges ($\Delta = 0$) versus the initial void volume fraction f_0 for $l/a = 0$, 0.0004, 0.001 and 0.002.

shock condition $\Delta = 0$ is not met, and the first maximum of the curve $\Delta - \xi$ is smoother (i.e. the curvature is smaller). The second maximum corresponds to the elastic wave front, that yields a discontinuity in the cavitation fields so that the condition $\Delta = 0$ is met for all values of the parameter l/a tested (see Cohen et al. [10]). Figure 4b presents the $\Delta - \xi$ curves for $f_0 = 0.05$ and $m = 0.17$. This value of m tends to m_c for $f_0 = 0.05$ and $l/a = 0$, so that the maximum of the $\Delta - \xi$ curve for $l/a = 0$ corresponds to the emerging plastic shock. Note that, unlike what occurs with the fully dense material (see Fig. 4a), the plastic shock does not emerge at the elastic/elastoplastic interface (which corresponds to the kink of the $\Delta - \xi$ curve located at $\xi \approx 3.1$), but it is located closer to the cavity wall, within the elastoplastic zone (see Fig. 1). Note also that the maximum of the $\Delta - \xi$ curves corresponding to $l/a > 0$ does not meet the condition $\Delta = 0$, showing that higher values of m are required for the plastic shock to emerge if size effects are accounted for (as anticipated in Fig. 2). Moreover, note that the elastic wave front ξ_e is located at $\xi > 4$ and thus it is not shown in the graph (recall that at the elastic wave front the condition $\Delta = 0$ is met irrespective of the value of l/a).

Figure 5 displays the evolution of the dimensionless plastic strain gradient $(\bar{\varepsilon}^p)'$ with the dimensionless radial coordinate ξ for $l/a = 0$, 0.0004, 0.001 and 0.002 (the same values of the dimensionless length scale parameter considered in Fig. 4). Results are shown for $f_0 = 0$, 0.01, 0.05 and 0.1 in subfigures (a), (b), (c) and (d), respectively. The cavity expansion velocity, for the four void volume fractions investigated, tends to the critical dimensionless velocity m_c of the size-independent material (i.e. for $l/a > 0$ a larger value of m is required for the plastic shock to be formed). The value of $(\bar{\varepsilon}^p)'$ first decreases as we move away from the cavity wall, reaches a local minimum, then increases until a maximum is attained for an intermediate value of ξ (corresponding to the plastic shock onset in the case of $l/a = 0$), and then decreases again, eventually dropping to zero right after the elastic/elastoplastic interface (which is identified in the plots as ξ_i). The comparison of the results for different void volume fractions shows that the value of $(\bar{\varepsilon}^p)'$ is generally smaller as the initial void volume fraction increases (notice that the scale of the y-axis of subfigures (a), (b), (c) and (d) is different). This is most likely because the value of m corresponding to subfigures (a), (b), (c) and (d) decreases as the porosity increases (since porosity promotes

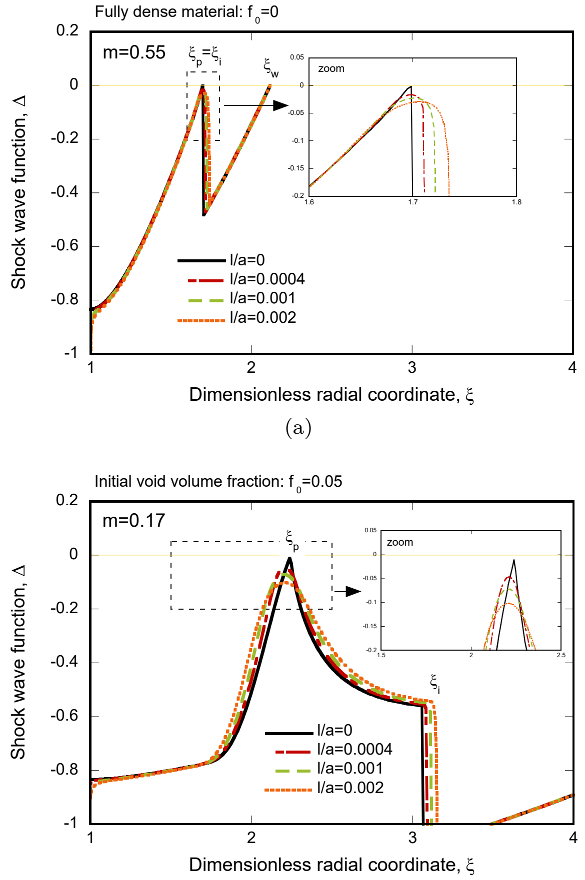

Figure 4: Shock wave function Δ versus dimensionless radial coordinate ξ for different values of the dimensionless length scale $l/a = 0$, 0.0004, 0.001 and 0.002. (a) Fully dense material $f_0 = 0$ and dimensionless velocity $m = 0.55$. (b) Initial void volume fraction $f_0 = 0.05$ and dimensionless velocity $m = 0.17$. The yellow line corresponds to the shock wave condition $\Delta = 0$. Recall that ξ_i denotes the elastic/elastoplastic interface and ξ_p the plastic shock location for $l/a = 0$.

plastic shock formation). On the other hand, for a given value of f_0, the only significant difference between the results obtained for different dimensionless length scale parameters is that the maximum of $(\bar{\varepsilon}^p)'$ that appears for an intermediate value of ξ is lower as l/a increases, bringing to light that size effects smooth the plastic strain gradients thus preventing discontinuities in the plastic strain field (i.e. hindering plastic shocks formation). These findings are in line with the results reported by Molinari and Ravichandran [35], who investigated plastic strain gradient effects on plastic shocks formation in periodic laminates and showed that, for a fixed stress amplitude, increasing the length scale parameter reduces the maximum plastic strain rate and increases the shock width. The length scale used in Molinari and Ravichandran [35] was related to the geometry of the layers and material characteristics of the constituents.

Figure 6 shows the dimensionless von Mises stress Σ_e versus the dimensionless radial coordinate ξ, for the same dimensionless length scale parameters, initial void volume fractions and cavity expansion velocities considered in Fig. 5. Notice that, while the plastic strain gradients near the cavity showed little dependence on the length scale parameter, see Fig. 5, the value of l/a has a significant influence on the von Mises stress fields that develop near the cavity, so that both the von Mises stress and the gradients of the von Mises stress increase as l/a increases. For the fully dense material, Fig. 6a, the elastic/elastoplastic interface, that in the case of $l/a = 0$ determines the location of the plastic shock (recall that for the

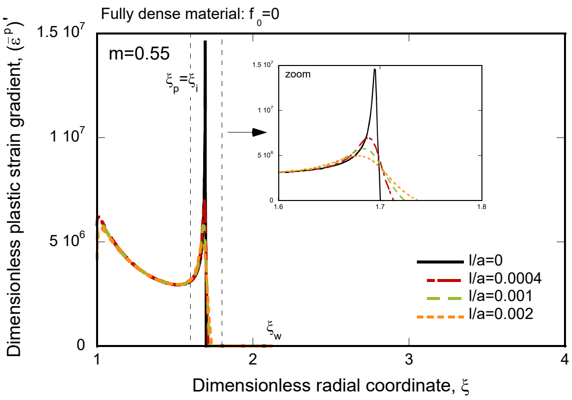

(a)

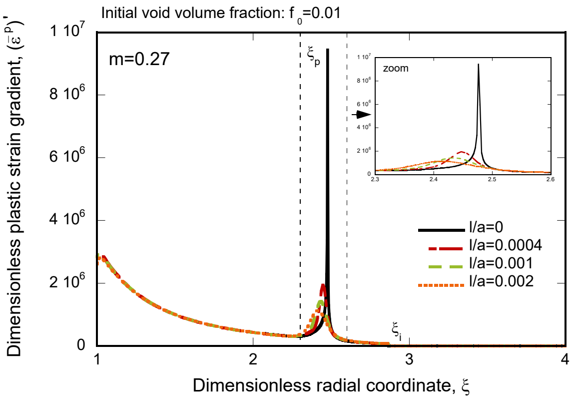

(b)

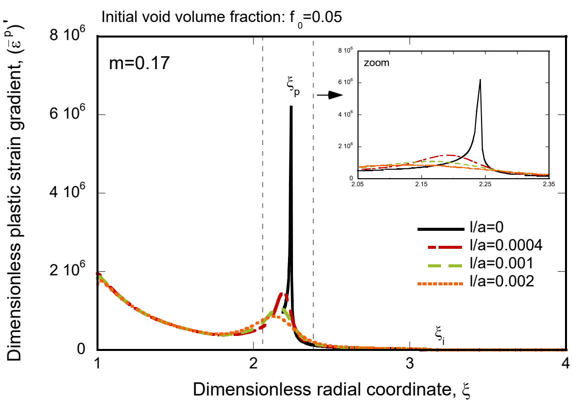

(c)

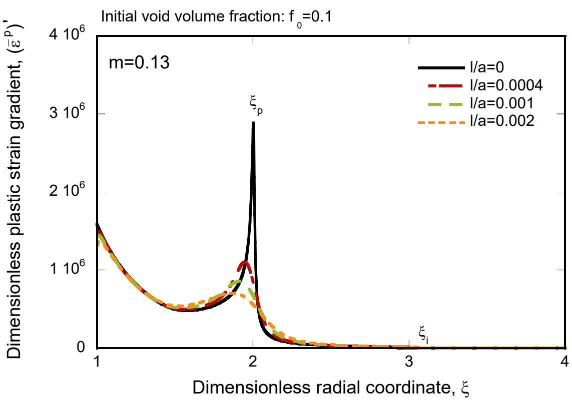

(d)

Figure 5: Dimensionless plastic strain gradient $(\bar{\varepsilon}^p)'$ versus dimensionless radial coordinate ξ for different values of the dimensionless length scale $l/a = 0$, 0.0004, 0.001 and 0.002. (a) Fully dense material $f_0 = 0$ and dimensionless velocity $m = 0.55$. (b) Initial void volume fraction $f_0 = 0.01$ and dimensionless velocity $m = 0.27$. (c) Initial void volume fraction $f_0 = 0.05$ and dimensionless velocity $m = 0.17$. (d) Initial void volume fraction $f_0 = 0.1$ and dimensionless velocity $m = 0.13$. Recall that ξ_i denotes the elastic/elastoplastic interface and ξ_p the plastic shock location for $l/a = 0$.

size-independent material the plastic shock emergence condition $\Delta \to 0$ has been met), leads to a sudden drop in the value of Σ_e which is more pronounced as the length scale parameter decreases. In contrast, for the porous materials, Figs. 6(b)-(c)-(d), the elastic/elastoplastic interface ξ_i corresponds to a kink in the $\Sigma_e - \xi$ curves, and the plastic shock ξ_p, that has emerged for $l/a = 0$ within the elastoplastic zone, is represented by a bump, i.e. a brief drop of Σ_e, which partially bounces back immediately after, and it is followed by a plateau that eventually extends until the elastic/elastoplastic interface. Notice that the bump is flatten with the increase of the length scale parameter, showing that size effects in porous materials prevent the formation of discontinuities in the von Mises stress fields within the elastoplastic zone, and thus the formation of plastic shocks (as mentioned before).

Figure 7 shows the evolution of the void volume fraction f with the dimensionless radial coordinate ξ, for the same dimensionless length scale parameters considered in Fig. 6, and three different values of the initial porosity $f_0 = 0.01$, 0.05 and 0.1. The values of the cavity expansion velocity are the same employed in Figs. 6 (b)-(c)-(d), namely $m = 0.27$, 0.17 and 0.13 in Figs. 7(a)-(b)-(c), respectively. The $f - \xi$ curves display a sigmoidal shape so that the porosity is zero near the cavity (the pores have closed), and $f = f_0$ for $\xi \geqslant \xi_i$ (no plastic deformation). The variation of the void volume fraction occurs within an intermediate range of values of ξ, near the radial coordinate corresponding to the plastic shock location for $l/a = 0$ (recall that for the values of m considered the plastic shock condition $\Delta \to 0$ has been met for the size-independent material). Notice that the slope of the $f - \xi$ curves increases as the dimensionless length scale parameter decreases, so that $f' \to \infty$ for the size independent material, showing that size effects prevent the formation of discontinuities in the porosity field.

5. Concluding remarks

The extension of the hypervelocity cavity expansion model of Cohen and Durban [9] to size-dependent materials developed by dos Santos et al. [41] has been used to determine the effect of size, induced by plastic strain gradient, on the formation of plastic shocks in porous materials. In particular, we have shown that the critical cavity expansion velocity for which plastic shocks emerge increases with the length scale parameter that controls the effect of size, and decreases with the material porosity, with the influence of porosity decreasing as the effect of size increases. In fact, investigation of the cavitation fields has shown that size effects act as a regularizing factor that tempers the gradients of plastic strain, thus hindering the formation of discontinuities in the field variables within the elastoplastic zone that develops near the cavity. Ultimately, the results presented in this paper shall be used to predict plastic shocks formation in hypervelocity nano-indentations. However, the validation of the theoretical predictions shown herein will be pending until relevant experimental results become available.

Acknowledgements

TdS wishes to acknowledge the support of FAPERGS, Fundação de Amparo à Pesquisa do Estado do Rio Grande do Sul, grant agreement $19/2551 - 0001054 - 0$.

JAR-M acknowledges the financial support obtained from the European Research Council (ERC) under the European

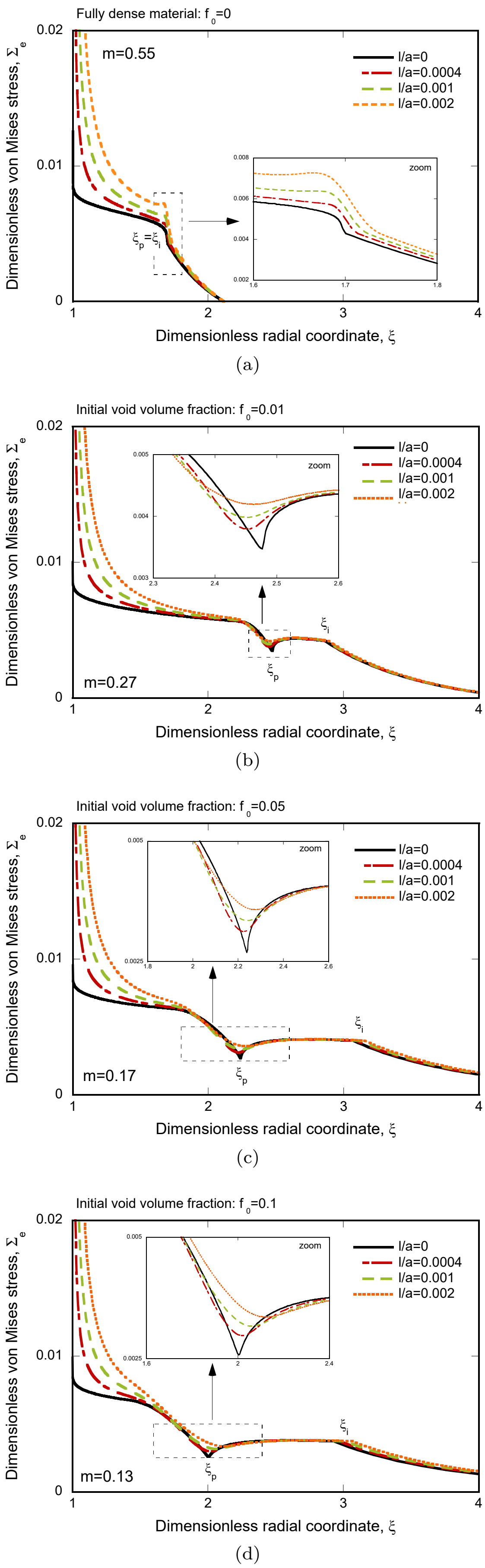

Figure 6: Dimensionless von Mises stress Σ_e versus dimensionless radial coordinate ξ for different values of the dimensionless length scale $l/a = 0$, 0.0004, 0.001 and 0.002. (a) Fully dense material $f_0 = 0$ and dimensionless velocity $m = 0.55$. (b) Initial void volume fraction $f_0 = 0.01$ and dimensionless velocity $m = 0.27$. (c) Initial void volume fraction $f_0 = 0.05$ and dimensionless velocity $m = 0.17$. (d) Initial void volume fraction $f_0 = 0.1$ and dimensionless velocity $m = 0.13$. Recall that ξ_i denotes the elastic/elastoplastic interface and ξ_p the plastic shock location for $l/a = 0$.

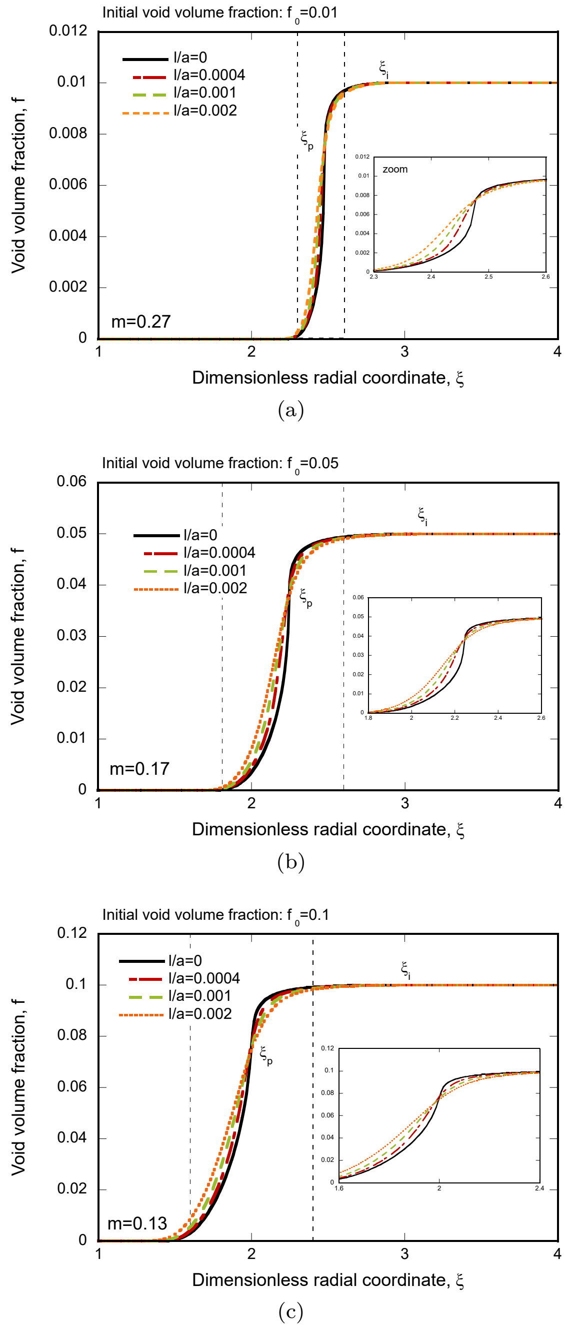

Figure 7: Void volume fraction f versus dimensionless radial coordinate ξ for different values of the dimensionless length scale $l/a = 0$, 0.0004, 0.001 and 0.002. (a) Initial void volume fraction $f_0 = 0.01$ and dimensionless velocity $m = 0.27$. (b) Initial void volume fraction $f_0 = 0.05$ and dimensionless velocity $m = 0.17$. (c) Initial void volume fraction $f_0 = 0.1$ and dimensionless velocity $m = 0.13$. Recall that ξ_i denotes the elastic/elastoplastic interface and ξ_p the plastic shock location for $l/a = 0$.

Union's Horizon 2020 research and innovation programme. Project PURPOSE, grant agreement 758056.

References

[1] Aboulkhair, N.T., Everitt, N.M., Ashcroft, I., Tuck, C., 2014. Reducing porosity in alsi10mg parts processed by selective laser melting. Additive Manufacturing 1-4, 77 – 86. Inaugural Issue.

[2] Aifantis, E.C., 1984. On the Microstructural Origin of Certain Inelastic Models. Journal of Engineering Materials and Technology 106, 326–330.

[3] Aifantis, E.C., 1992. On the role of gradients in the localization of deformation and fracture. International Journal of Engineering Science 30, 1279 – 1299.

[4] Aifantis, E.C., 1995. Pattern formation in plasticity. International Journal of Engineering Science 33, 2161 – 2178. The Edelen Symposium.

[5] Arreguin-Zavala, J., Milligan, J., Davies, M.I., Goodes, S.R., Brochu, M., 2013. Characterization of nanostructured and ultrafine-grain aluminum-silicon claddings using the nanoimpact indentation technique. The Journal of The Minerals, Metals & Materials Society 65, 763–768.

[6] Bashurov, V.V., Bebenin, G.V., Belov, G.V., Bukharev, Y.N., Zhukov, V.I., Ioilev, A.G., Lapichev, N.V., Mikhailov, A.L., Smirnov, G.S., Fateev, Y.A., Schlyapnikov, G.P., 1997. Experimental modelling and numerical simulation of high- and hypervelocity space debris impact to spacecraft shield protection. International Journal of Impact Engineering 20, 69 – 78. Hypervelocity Impact Proceedings of the 1996 Symposium.

[7] Chen, J., Yuan, H., 2002. A micro-mechanical damage model based on gradient plasticity: algorithms and applications. International Journal for Numerical Methods in Engineering 54, 399–420.

[8] Cleja-Tigoiu, S., Cazacu, O., Tigoiu, V., 2008. Dynamic expansion of a spherical cavity within a rate-dependent compressible porous material. International Journal of Plasticity 24, 775 – 803.

[9] Cohen, T., Durban, D., 2013. Hypervelocity cavity expansion in porous elastoplastic solids. Journal of Applied Mechanics 80, 011017.

[10] Cohen, T., Masri, R., Durban, D., 2010. Shock waves in dynamic cavity expansion. Journal of Applied Mechanics 77, 041009.

[11] Cowles, B., 1996. High cycle fatigue in aircraft gas turbines-an industry perspective. International Journal of Fracture 80, 147–163.

[12] Czarnota, C., Molinari, A., Mercier, S., 2017. The structure of steady shock waves in porous metals. Journal of the Mechanics and Physics of Solids 107, 204 – 228.

[13] Czarnota, C., Molinari, A., Mercier, S., 2020. Steady shock waves in porous metals: Viscosity and micro-inertia effects. International Journal of Plasticity 135, 102816.

[14] Danas, K., Deshpande, V.S., Fleck, N.A., 2012. Size effects in the conical indentation of an elasto-plastic solid. Journal of the Mechanics and Physics of Solids 60, 1605 – 1625.

[15] Drucker, D.C., 1979. Approximate calculations of spall and cratering in high speed impact, in: Kawata, K., Shioiri, J. (Eds.), High Velocity Deformation of Solids, Springer Berlin Heidelberg, Berlin, Heidelberg. pp. 214–227.

[16] Durban, D., Masri, R., 2004. Dynamic spherical cavity expansion in a pressure sensitive elastoplastic medium. International Journal of Solids and Structures 41, 5697–5716.

[17] Fleck, N., Hutchinson, J., 1997. Strain gradient plasticity, Elsevier. volume 33 of *Advances in Applied Mechanics*, pp. 295 – 361.

[18] Fleck, N., Otoyo, H., Needleman, A., 1992. Indentation of porous solids. International Journal of Solids and Structures 29, 1613 – 1636.

[19] Forrestal, M.J., Brar, N.S., Luk, V.K., 1991. Penetration of strain-hardening targets with rigid spherical-nose rods. Journal of Applied Mechanics 58, 7–10.

[20] Gao, X.L., Jing, X., Subhash, G., 2006. Two new expanding cavity models for indentation deformations of elastic strain-hardening materials. International Journal of Solids and Structures 43, 2193 – 2208.

[21] Ghosh, A., Jin, S., Arreguin-Zavala, J., Brochu, M., 2017. Characterization and investigation of size effect in nano-impact indentations performed using cube-corner indenter tip. Journal of Materials Research 32, 2241–2248.

[22] Goodier, J., 1965. On the mechanics of indentation and cratering in solid targets of strain-hardening metal by impact of hard and soft spheres, in: Proceedings of the 7th Symposium on Hypervelocity Impact, pp. 215–259.

[23] Gurson, A.L., 1977. Continuum theory of ductile rupture by void nucleation and growth. Part I: Yield criteria and flow rules for porous ductile media. ASME Journal of Engineering Materials and Technology 99, 2–15.

[24] Hassani, M., Veysset, D., Nelson, K.A., Schuh, C.A., 2020. Material hardness at strain rates beyond 106 s-1 via high velocity microparticle impact indentation. Scripta Materialia 177, 198 – 202.

[25] Heidari, L., Tangestani, A., Hadianfard, M.J., Vashaee, D., Tayebi, L., 2020. Effect of fabrication method on the structure and properties of a nanostructured nickel-free stainless steel. Advanced Powder Technology 31, 3408 – 3419.

[26] Hopkins, H., 1960. Dynamic expansion of spherical cavities in metals. Progress in Solid Mechanics 1, 5–16.

[27] Johnson, K.L., 1970. The correlation of indentation experiments. Journal of the Mechanics and Physics of Solids 18, 115 – 126.

[28] Lu, J., Suresh, S., Ravichandran, G., 2003. Dynamic indentation for determining the strain rate sensitivity of metals. Journal of the Mechanics and Physics of Solids 51, 1923 – 1938. Proceedings of a Symposium on Dynamic Failure and Thin Film Mechanics, honoring Professor L.B. Freund.

[29] Masri, R., 2016. Cavitation in solids and ballistic limit predictions for perforation of metal targets by nose-pointed projectiles, in: Proceedings of the 34th Israeli Conference of Mechanical Engineering.

[30] Masri, R., Durban, D., 2005. Dynamic spherical cavity expansion in an elastoplastic compressible mises solid. Journal of Applied Mechanics 72, 887–898.

[31] Masri, R., Durban, D., 2009. Deep penetration analysis with dynamic cylindrical cavitation fields. International Journal of Impact Engineering 36, 830 – 841.

[32] McElhaney, K.W., Vlassak, J.J., Nix, W.D., 1998. Determination of indenter tip geometry and indentation contact area for depth-sensing indentation experiments. Journal of Materials Research 13, 1300–1306.

[33] Mok, C., Duffy, J., 1964. The behavior of metals at elevated temperatures under impact with a bouncing ball. International Journal of Mechanical Sciences 6, 161 – 175.

[34] Molinari, A., Ravichandran, G., 2004. Fundamental structure of steady plastic shock waves in metals. Journal of Applied Physics 95, 1718–1732.

[35] Molinari, A., Ravichandran, G., 2006. Modeling plastic shocks in periodic laminates with gradient plasticity theories. Journal of the Mechanics and Physics of Solids 54, 2495–2526.

[36] Nix, W.D., Gao, H., 1998. Indentation size effects in crystalline materials: A law for strain gradient plasticity. Journal of the Mechanics and Physics of Solids 46, 411 – 425.

[37] Poole, W.J., Ashby, M.F., Fleck, N.A., 1996. Micro-hardness of annealed and work-hardened copper polycrystals. Scripta Materialia 34, 559 – 564.

[38] Qin, L., Li, H., Shi, X., Beake, B.D., Xiao, L., Smith, J.F., Sun, Z., Chen, J., 2019. Investigation on dynamic hardness and high strain rate indentation size effects in aluminium (110) using nano-impact. Mechanics of Materials 133, 55 – 62.

[39] dos Santos, T., Brezolin, A., Rossi, R., Rodríguez-Martínez, J.A., 2020. Modeling dynamic spherical cavity expansion in elasto-viscoplastic media. Acta Mechanica 231, 2381–2397.

[40] dos Santos, T., N'souglo, K.E., Rodríguez-Martínez, J.A., 2019. Dynamic spherical cavity expansion in Gurson materials with uniform and non-uniform distributions of porosity. Mechanics of Materials 134, 115–131.

[41] dos Santos, T., Srivastava, A., Rodríguez-Martínez, J.A., 2021. The combined effect of size, inertia and porosity on the indentation response of ductile materials. Mechanics of Materials 153, 103674.

[42] Srivastava, A., Ponson, L., Osovski, S., Bouchaud, E., Tvergaard, V., Needleman, A., 2014. Effect of inclusion density on ductile fracture toughness and roughness. Journal of the Mechanics and Physics of Solids 63, 62–79.

[43] Subhash, G., Koeppel, B.J., Chandra, A., 1999. Dynamic Indentation Hardness and Rate Sensitivity in Metals. Journal of Engineering Materials and Technology 121, 257–263.

[44] Thompson, M.K., Moroni, G., Vaneker, T., Fadel, G., Campbell, R.I., Gibson, I., Bernard, A., Schulz, J., Graf, P., Ahuja, B., Martina, F., 2016. Design for additive manufacturing: Trends, opportunities, considerations, and constraints. CIRP Annals 65, 737 – 760.

[45] Tirupataiah, Y., Sundararajan, G., 1991. A dynamic indentation technique for the characterization of the high strain rate plastic flow behaviour of ductile metals and alloys. Journal of the Mechanics and Physics of Solids 39, 243 – 271.

[46] Trelewicz, J.R., Schuh, C.A., 2008. The hall-petch breakdown at high strain rates: Optimizing nanocrystalline grain size for impact applications. Applied Physics Letters 93, 171916.

[47] Tsagrakis, I., Konstantinidis, A., Aifantis, E.C., 2003. Strain gradient and wavelet interpretation of size effects in yield and strength. Mechanics of Materials 35, 733 – 745. Special Issue: Multi-scale modeling of materials.

[48] Tvergaard, V., 1981. Influence of voids on shear band instabilities under plane strain conditions. International Journal of Fracture 17,

389–407.

[49] Tvergaard, V., 1982. On localization in ductile materials containing spherical voids. International Journal of Fracture 18, 237–252.

[50] Zhu, L., Li, N., Childs, P., 2018. Light-weighting in aerospace component and system design. Propulsion and Power Research 7, 103 – 119.

[51] Zukas, J.A., Segletes, S., 1992. Numerical modeling of hypervelocity impact phenomena with desktop computers. Advances in Engineering Software 14, 77 – 84.